XRF and hyperspectral analyses as an automatic way to detect flood events in sediment cores

William Rapuc, Kevin Jacq, Anne-Lise Develle, Pierre Sabatier, Bernard Fanget, Yves Perrette, Didier Coquin, Maxime Debret, Bruno Wilhelm, Fabien Arnaud

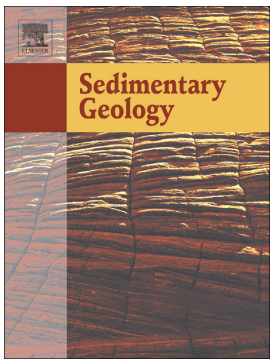

XRF and hyperspectral analyses as an automatic way to detect flood events in sediment cores

William Rapuc, Kévin Jacq, Anne-Lise Develle-Vincent, Pierre Sabatier, Bernard Fanget, Yves Perrette, Didier Coquin, Maxime Debret, Bruno Wilhelm, Fabien Arnaud

PII: S0037-0738(20)30191-3

DOI: https://doi.org/10.1016/j.sedgeo.2020.105776

Reference: SEDGEO 105776

To appear in: *Sedimentary Geology*

Received date: 22 July 2020

Revised date: 21 September 2020

Accepted date: 22 September 2020

Please cite this article as: W. Rapuc, K. Jacq, A.-L. Develle-Vincent, et al., XRF and hyperspectral analyses as an automatic way to detect flood events in sediment cores, *Sedimentary Geology* (2020), https://doi.org/10.1016/j.sedgeo.2020.105776

XRF and hyperspectral analyses as an automatic way to detect flood events in sediment cores

William Rapuc (1), Kévin Jacq (1, 2), Anne-Lise Develle-Vincent (1), Pierre Sabatier (1), Bernard Fanget (1), Yves Perrette (1), Didier Coquin (2), Maxime Debret (3) Bruno Wilhelm (4) et Fabien Arnaud (1)

(1) Université Grenoble Alpes, Université Savoie Mont Blanc, CNRS, EDYTEM, LE Bourget du lac, France

(2) Université Savoie Mont Blanc, LISTIC, 74944 Annecy Le Vieux, France

(3) Université De Caen, CNRS, LM2C, 76821 Mont-Saint-Aignan, France

(4) Institute for Geosciences and Environmental research (IGE), UGA, CNRS, IRD,Grenoble, France

Corresponding Author:

William Rapuc

UMR CNRS 5204 Environnements, Dynamiques et Territoires de la Montagne (EDYTEM)

Université Savoie Mont Blanc, Campus scientifique,

73376 Le Bourget du Lac cedex, France

william.rapuc@univ-smb.fr

Abstract

Long-term changes in flood activity have often been reconstructed to understand their relationships to climate changes. This requires identification of flood layers according to certain characteristics (e.g., texture, geochemical composition, grain-size) and then to count them using naked-eye observation. This method is, however, time-consuming, and intrinsically characterized by a low

resolution that may lead to bias and misidentification. To overcome this limitation, high-resolution analytical approaches can be used, such as X-ray fluorescence spectroscopy (XRF), X-ray computed tomography, or hyperspectral imaging (HSI). When coupled with discriminant algorithms, HSI allows for automatic identification of event layers. Here, we propose a new method of flood layers identification and counting based on the combination of both HSI and XRF core scanner analyses, applied to a Lake Bourget (French Alps) sediment sequence. We use a hyperspectral sensor from the short wave-infrared spectral range to create a discrimination model between event layers and continuous sedimentation. This first step allows the estimation of a classification map, with a prediction accuracy of 0.96, and then the automatic reconstruction of a reliable chronicle of event layers (including their occurrence and deposit thicknesses). XRF signals are then used to discriminate flood layers among all identified event layers based on site-specific geochemical elements (in the case of Lake Bourget: Mn and Ti). This results in an automatically generated flood chronicle. Changes in flood occurrence and event thickness through time reconstructed from the automatically generated floods chronicle are in good agreement with the naked-eye-generated chronicle. In detail, differences rely on a larger number of detected flood events (i.e., increase of 9% of the number of layers detected) and a more precise layer thickness estimation, thanks to a higher resolution. Therefore, the developed methodology opens a promising avenue to increase both the efficiency (timesaving) and robustness (higher accuracy) of paleoflood reconstructions from lake sediments. Also, this methodology can be applied to identify any specific layers (e.g., varve, tephra, mass-movement turbidite, tsunami) and, thereby, it has a direct implication in paleolimnology, paleoflood hydrology and paleoseismology from sediment archives.

Keywords

Lake sediment, hyperspectral analyses, XRF geochemical analysis, Automatic flood chronicle

1. Introduction

Changes in flood occurrence and magnitude are expected due to climate change in many regions, affecting an increasing number of people (Hirabayashi et al., 2013; Blöschl et al., 2019). Large uncertainties still exist on such changes and long-term flood records are of high value to fully understand climate-flood relationships (Merz et al., 2014; Wilhelm et al., 2019). To this end, numerous studies are undertaken on geological records such as lake sediments to reconstruct centennial to millennial flood records (Noren et al., 2002; Moreno et al., 2008; Giguet-Covex et al., 2012; Wilhelm et al., 2012, 2017; Glur et al., 2013; Wirth et al., 2013; Sabatier et al., 2017; Corella et al., 2019; Rapuc et al., 2019). Flood events produce turbidity currents in the lake basin that will usually lead to a normally graded detrital layer that differs from the surrounding continuous sedimentation (Sturm and Matter, 1978; Gilli et al., 2013). However, other processes such as earthquakes, spontaneous delta front collapses, and lake-level changes, can also produce turbidity currents in lakes (Sauerbrey et al., 2013; Wilhelm et al., 2017; Rapuc et al., 2018). In most of these studies, to count and differentiate the event layers, the sediment facies are first described visually, then several sedimentological and geochemical analyses are undertaken. From those results, the event layers are identified, allowing the interpretation of a potential trigger. Then, layers with the same characteristics are usually identified and counted all along the core by naked-eye observation to ultimately produce a flood chronicle. Those methods are, however, time-consuming, have a low spatial resolution potential, and they can be destructive (e.g., through grain-size measurements, total organic carbon analyses). More importantly, naked-eye identification and counting can lead to inaccuracy and misidentification due to human bias and intrinsic low resolution. To overcome this limitation, an automatic layer detection method coupled to a high-resolution analysis is required and would also allow results to be fully reproducible.

As several parameters such as color, texture, grain-size and chemical composition vary between flood events and the continuous sedimentation in a lake, we propose to go further than Vannière et

al., (2013) who first proposed an automatic way to detect events layers based on RGB images. In this study, we explore the use of short-wave infrared hyperspectral imaging (HSI) applied on the Lake Bourget (France) sediment sequence. HSI has shown potential to highlight organic matter (Butz et al., 2017; Schneider et al., 2018; Speta et al., 2018; Van Exem et al., 2018; Jacq et al., 2019b), mineral compounds (Lampinen et al., 2019; Tusa et al., 2019) and particle size (Jacq et al., 2019a) in lake sediments. The partial least squares discriminant analysis (PLS-DA) was used to discriminate event layers from continuous sedimentation, as presented in a previous study (Jacq et al., 2020). This results in an event layer chronicle including depth and thickness for each event layer with a 200 µm resolution. In a second step, XRF element geochemistry performed with an Avaatech core-scanner analyses with a high resolution of 500 µm are used to interpret the trigger of the event layers and create a flood chronicle. To test the accuracy of this new method, we compare our results to a naked-eye flood chronicle for the same core.

2. Study Site

Lake Bourget (18 km long, 2.8 km wide, 231.5 m.a.s.l) is one of the largest natural lake in France (44.5 km²). This lake is a peri-alpine hard water lake located in the northwestern part of the French Alps (Fig. 1) and was formed by the retreat of Würmian glaciers (Nicoud et al., 1987). Three tributaries enter Lake Bourget: Leysse, Sierroz and the Rhône rivers (Fig. 1). The Rhône river is usually the outflow of Lake Bourget, but current reversal takes place during flood events and inflows in the lake. Including the Rhône River catchment, the catchment of Lake Bourget covers a large area (approx. 4600 km²) and diverse lithologies including granitic rocks of the Mont Blanc massif as well as Cretaceous limestones. Lake Bourget is a monomictic lake that presents a partial reoxygenation of its hypolimnion during winter water mixing followed by hypoxia that increases progressively during thermal stratification (Jenny et al., 2013). For most of the year, the bottom water of the lake thus presents low oxygen concentration compared to surface water and river water input. The sediments of Lake Bourget have already been studied to understand the history of the lake eutrophication

(Giguet-Covex et al., 2010; Jenny et al., 2013), and regional flood activity (Chapron et al., 2002, 2005; Arnaud et al., 2005; Debret et al., 2010; Jenny et al., 2014; Evin et al., 2019), to characterize the evolution of erosion in the watershed (Revel-Rolland et al., 2005; Arnaud et al., 2012) or to study seismically induced deposits (Chapron et al., 1999). From all those studies, it appears that the northern part of the lake basin is influenced by flood events from the Rhône River, contributing from 10 to 40% to the total sedimentation, and can generate event layers due to underflows during high-energy flood events (Giguet-Covex et al., 2010; Arnaud et al., 2012).

The continuous background sedimentation in the Northern part of Lake Bourget is mainly composed of an alternation of very dark grey and very light grey clayey laminae over the first centimeters with a predominance of diatoms, authigenic calcite crystals and organic matter (Giguet-Covex et al., 2010). This upper part presents the highest TOC values, i.e., 2.5% (Millet et al., 2010) and results from the eutrophication of the lake initiated in the middle of the 20th century (Debret et al., 2010; Giguet-Covex et al., 2010; Jenny et al., 2013). The sediment composition evolves downwards, authigenic carbonates remain the major component but the concentration in detrital particles increase associated to a progressive decrease of TOC values (Debret et al., 2010; Millet et al., 2010).

The deposits linked to flood events in the proximal part of the Lake Bourget basin are characterized by a dark to very dark grey color (10 YR 4/1, Munsell soil color chart) and are easily distinguishable from the light grey continuous background sedimentation (Giguet-Covex et al., 2010). The thickness of these deposits varies from millimeter to centimeter scale. These fine-silty to clayey deposits are mainly composed of allochthonous silicates and enriched in detrital elements (Giguet-Covex et al., 2010; Jenny et al., 2014). Some homogenite-type deposits were also observed in the sediment of Lake Bourget and correspond to light grey deposits rich in autochthonous carbonates (Chapron et al., 1999). Arnaud et al. (2012) showed that the Ti signal, from XRF data, is the best proxy to represent detrital input in Lake Bourget. Jenny et al. (2014) and Evin et al. (2019) evidenced that the flood-

sediment pathways are always changing in Lake Bourget, which explains why grain-size is not used as a proxy of flood deposits.

3. Materials and Methods

3.1. Coring and lithological description

In 2017, a sediment core (LDB17-P11, length 271 cm) was retrieved from the northern basin of Lake Bourget (45° 46.778'N, 5° 50.552'E, 113 m water depth, Fig. 1) using a UWITEC gravity corer with a hammer. This site was selected because it is highly influenced by the detrital sediment input from the Rhône River (Jenny et al., 2014). The section was cut in two parts (A & B), split in half, photographed at high resolution (20 pixels mm^{-1}), and described and logged in detail using the Munsell color chart. Therein, the study focuses on the upper section (LDB17-P11A - 121.5 cm) that presents the highest number of event layers. The sediment retrieved in the LDB17-P11A sediment core can be subdivided into two different units (Fig. 2). The upper part (0 - 10.4 cm depth) of the core composed of dark-greenish-grey clay (5GY 4/4) presents a thin alternation of dark grey, light grey and brown laminae and is equivalent to the one observed and described previously in Lake Bourget by Giguet-Covex et al. (2010) and Jenny et al. (2013). This unit corresponds to a laminated organic gyttja linked to recent eutrophication of the bottom water of Lake Bourget (Giguet-Covex et al., 2010; Jenny et al., 2013). The second unit (10.4 – 121.5 cm depth) is characterized by a homogeneous clayey to silty light grey sediment that is predominantly composed of carbonate particles and a few diatoms. This unit is often interrupted by darker deposits, rich in detrital compounds (silicate and carbonate) that were previously interpreted as turbidite-type deposits induced by underflow linked to flood events incoming from the Rhône river (Giguet-Covex et al., 2010; Jenny et al., 2014).

3.2. Spectroscopic analysis

Two non-destructive high-resolution spectroscopic methods were applied to the sediment core. The Short Wave Infrared (SWIR) and XRF were used to estimate the molecular and elementary properties of event layers.

3.2.1. Hyperspectral analysis

The SWIR sensor covers the spectral range from 1000 nm to 2500 nm with 12 nm bandwidth, so that the spectra is composed of 144 spectral bands, and the spatial resolution at sampling is 200 µm. Hyperspectral acquisition protocols proposed by Butz et al. (2015) and Jacq et al. (2020) were followed and they are composed of three main steps : (1) The sample needs to be prepared to be as flat as possible and reveal sedimentary structures ; (2) both camera and scanner must be adjusted to obtain squared pixels and an optimal signal to noise ratio ; and (3) the data must be calibrated with the white (spectralon) and dark (shutter closed) normalizations to obtain the reflectance spectra of the sample.

Several pre-processing steps can be used to remove noise or highlight discriminant spectral information. Spectral detrending (Barnes et al., 1989) was used to correct the spectra from the baseline as chosen in a previous study (Jacq et al., 2020).

3.2.2. Geochemical properties

XRF geochemical analysis was performed on the EDYTEM laboratory's Core Scanner (Avaatech XRF Technology) to characterize the variations of major elements throughout LDB17-P11A sediment sequence. A continuous 0.5 mm step measurement was applied with a run at 10 kV and 0.25 mA for 20 s to detect lightweight elements, such as Al, Si, K, Ca, Ti, and a second run was performed at 30 kV and 0.4 mA for 20 s to detect Mn, Fe, Br, Rb, Sr, and Zr. The XRF core scanner results are expressed hereafter as peak intensities by counts per second (cps). Then, a principal component analysis (PCA) was conducted on the XRF data to identify principal sediment end-members and correlations between the detected elements (Sabatier et al., 2010). Due to the 500 µm resolution, only the layers

thicker than 0.5 mm can be detected with XRF data, and only layers thicker or equal to 1 mm will be described to increase the reliability of the study.

3.3. The methodology of detection and interpretation of event layers

To detect and interpret the event layers present in a sediment core we used a combination of HSI and XRF that can be summarized as follows (Fig. 2): (i) Opening and visual description of the core to identify and count the different types of event layers; (ii) Hyperspectral analysis associated with data treatment and the selection by the user of some event layers as reference layers to produce a chronicle; (iii) Perform XRF analysis at high-resolution; (iv) From knowledge of the in-lake sedimentary processes, using previous researches and/or sedimentological and geochemical analyses (XRD, energy dispersive X-ray spectroscopy, XRF, grain-size, anisotropy of magnetic susceptibility), selection of one proxy of detrital input, one proxy of grain-size or transport processes, and if needed one proxy of oxygenation of the lake bottom water from XRF data; and (v) Combination of hyperspectral chronicle and XRF data to create (vi) an interpreted flood chronicle and calculate the thicknesses of each flood layer. The main step of this method will be developed hereafter. All these steps were processed in Matlab software (R2020a), using the following method: https://github.com/JacqKevin/HSI_SupervisedClassification.

3.3.1. Hyperspectral classification and event layer chronicle estimation

First, data need to be manually labelled to create a training dataset. This requires that a user manually select rectangles on a pseudo-RGB image that correspond to reference event layers or continuous sedimentation layers. The selected pixels are then extracted to create a calibration set to estimate the classification model parameters and produce a validation set to test its performances. A PLS-DA is used for classification modelling (Wold et al., 1984; Barker and Rayens, 2003). This method is based on the PLS approach that reduces the spectral data in latent variables maximizing the spectral variability and the co-variability between the spectra and variables of interest. The model performances are estimated with the calibration and prediction accuracies that estimate the ratio of

pixels that are successfully classified into their corresponding classes. A qualitative assessment is also realized to check the accuracy of the prediction map. The optimal classification model allows discriminating the event layers from the continuous sedimentation with a classification map (Fig. 3).

Based on a previous study of Jacq et al. (2020), hyperspectral classification can discriminate event layers from continuous sedimentation with the SWIR image. A discrimination model was estimated (Fig. 3) and presents a calibration accuracy of 0.97, validation accuracy of 0.96, and qualitative relevance of 5/5.

Then, a summed profile of the classification map is calculated, normalized by the number of width pixels, it can be seen as the occurrence probability of an event (Fig. 3). This profile was smoothed to remove artifacts and mis-classifications with a Savitzky-Golay filter (Savitzky and Golay, 1964). A double threshold was fixed to find the event layer boundaries and to create the chronicle. The first threshold was set at 50% of the width. It allowed us to find thin and thick deposits without selecting artifacts or mis-classification, but thicker deposits (greater than 5 mm) can result from the amalgamation of several close layers. The second threshold at 15% of the width was used to divide the deposits. Finally, each deposit can be separated, and their depth and thickness estimated to create an event layer chronicle without information about event triggers. In some lake environments, the thickness of flood layers may be informative about flood intensity (Wilhelm et al., 2013, 2019; Sabatier et al., 2017) but it is not the case in Lake Bourget. Here, thickness estimation is thus only considered for further applications on other lakes. Hence, a cumulative sum was also calculated to test the accuracy of an automatic model on the detection of the number and thickness of event layers. Therein, only layers with thickness greater than 1 mm are used because this represents the resolution limit used to build the naked-eye chronicle, and the XRF analysis resolution did not allow for characterization of thinner deposits. Once the method is validated, the event layer chronicle can be exploited at the limit of XRF data resolution.

3.3.2. Flood proxies derived from XRF

In a lake system, several mechanisms can trigger an event layer : (i) lake level fluctuations, (ii) snow avalanches, (iii) eruptions, (iv) sediment overloading on slopes or deltas, (v) destabilization of slopes and deltas by seismic shaking, and (vi) flood events (e.g., Sauerbrey et al., 2013; Rapuc et al., 2018). Regardless of the lake system considered, to discriminate the triggering mechanisms of each deposit it is necessary to select a combination of proxies allowing for interpretation of (1) the sources and (2) the grain-size of the sediment composing the event layers and (3) the transport processes leading to deposition of the sediment. Here we focused only on a way to discriminate flood layers from surrounding sedimentation using XRF signals, but this method can apply to any other triggers. Floods induce an input of sediment rich in detrital material coming from the watershed, and they generally produce a turbiditic underflow in the lake, leading to sediment sorting and deposition of a graded layer (Sturm and Matter, 1978). When the oxygen-rich water, coming from the watershed during a flood, reaches the water-sediment interface due to an underflow, the Mn and Fe present in dissolved form precipitate as Mn and Fe oxy-hydroxides at the base of the induced turbiditic layer. Thus, a peak of Mn or Fe can be interpreted as flood-induced lake bottom oxygenation and is linked to detrital input (Wilhelm et al., 2016; Sabatier et al., 2017; Rapuc et al., 2019). However, changes in the oxic/anoxic state of the bottom water of the lake will also lead to similar changes in Fe and Mn (Davison, 1993; Elbaz-Poulichet et al., 2014). Because it can be affected by oxic and reduction processes, Fe does not seem to be a good proxy to trace detrital input from flood events and will not be used in this study. Thus, ratios such as Zr/Fe, used to represent grain-size variations in lake sediment and interpreted as a proxy of grain size (Wilhelm et al., 2013) should not be used with much confidence when studying a flood deposit in lakes influenced by changes in the oxygenation of lake bottom water. Depending on lake mechanics and the available knowledge, the user can select one or several proxies to interpret event layers.

3.3.3. XRF flood proxies and HSI chronicle combination

The selected XRF profiles were smoothed to reduced noise with a Savitzky-Golay filter (Savitzky and Golay, 1964). Then, all the peaks were detected with local maxima. Some constraints can be used with the peak height, prominence, width, and distance between two consecutive peaks, but no such constraint was used in this study. Finally, a depth matching of the HSI event layers and the XRF profiles was made. For each event layer detected by HSI, the presence or absence of XRF peaks in this area will characterize the type of event. Thus, the instantaneous chronicle made by HSI was interpreted thanks to the XRF to obtain a chronicle by type of each event.

3.3.4. Comparison with the naked eye chronicle

The comparison of the two (HSI+XRF and naked-eye) chronicles relied on results of event frequency and cumulative thickness calculated as the sum of the number of deposits counted every 10 cm and the cumulative thickness of the deposits, respectively. Then correlation and standard error were calculated to measure similarity and distance between the naked-eye and estimated chronicles. A quantile-quantile plot was also used to compare the respective distributions in depth and thickness.

4. Results

4.1. Visual description of the core and naked-eye chronicle

Event layers, characterized by a dark to very dark grey color (10 YR 4/1), were counted visually along the LDB17-P11A sediment core (Fig. 2). As these layers are easily distinguishable from continuous sedimentation, we counted all the deposits with a thicknesses ≥ 1 mm. To improve the accuracy of our results, the counting of these deposits was repeated by another observer. Fifty-six event layers were counted, with a maximum thickness of 11.0 mm and a mean thickness of 3.4 mm. One other deposit, interrupting the continuous sedimentation, was identified between 31.5 and 32.1 cm deep (Figs. 3, 4). This deposit is composed of light grey silty to clayey sediment rich in carbonates and corresponds to a homogenite-type deposit linked to a seismic event that occurs close to the lake in

1822 (Chapron et al., 1999). To build a flood chronicle, the homogenite-type deposit was removed, and the sum of the number of deposits counted every 10 cm and the cumulative thickness of the deposits was plotted against the depth of the core.

4.2. Hyperspectral analyses

On the LDB17-P11 section, 21 rectangles were selected in approximately 5 minutes, covering 1.20 % of the total section area. From this selection, an HSI discrimination model was built on the entire sequence, allowing the estimation of a chronicle (Fig. 4), with the depth and thickness of each layer. However, the model cannot distinguish between turbidite-type and homogenite-type deposits (Fig. 3). Thus, the hyperspectral model cannot be used directly to classify the different kinds of events layers and discuss their origin. One hundred and ten deposits were counted using the SWIR camera, 86 have a thickness greater than 1 mm, and are used hereafter. These present a mean thickness of 4.5 mm and a maximum thickness of 15.5 mm.

4.3. High-resolution XRF analyses

From the XRF analyses, Unit I shows low values of Ti [> 3 kilo counts per second (kcps)], Fe (> 100 kcps), and K (> 9 kcps) and high values of Ca (> 145 kcps). From the top of the sediment section to the base of Unit II, the Ti, K, Fe, and Mn signals increase (Fig. 4). The Ca signal is quite constant over the first 121 cm of the LDB17-P11A sediment core. The event layers present peaks of Ti, Fe, Mn, and K and low values of Ca (Fig.4). The Zr/K ratio presents important peaks at the base of each event layer and low values at the top (Fig. 4). The only homogenite-type deposit identified in the core section presents relatively low values of Ti, Fe, and K and show a relatively high value of Ca and Mn signal. A peak of Zr/K is present at the base of this deposit. The variability of the Mn and Fe signal increases downward (Fig. 4).

From the XRF data, a PCA was conducted and provides variables and individual factor maps (Fig. 5), which highlight the relationships between the different elements and geochemical distributions within sediment units. Dimensions 1 and 2 (denoted as Dim1 and Dim2) represent 73.9% of the total

variability of the signal. From the variables factor map, three end-members were identified. The first, which is denoted as terrigenous, is positively correlated with Dim1 and yields high positive loadings for the major terrigenous elements (Zr, Fe, Ti, Rb, Mn, Al, Si, and K). This pole can be subdivided into two-parts, (i) the upper part including Zr, Fe, Rb, Ti, and Mn, that are particles usually linked to coarse grains or reduction–oxidation processes in lake sediment (Davies et al., 2015 and references therein), and (ii) the lower part including Al, Si and K. The second end-member, which is denoted as "organic matter" yields positive values for Br and is negatively correlated with Dim1 and positively with Dim2. The third end-member is negatively correlated with Dim1 and with Dim2 (Fig. 5A). This pole yields high positive values for Ca and is interpreted as representing carbonates produced by biologic activity in the lake, as Sr is usually present in marine limestone that constitutes a significant part of the outcrops in the watershed of Lake Bourget, and is here anticorrelated with Ca. The individual factor map (Fig. 5B) identifies specific features in each unit. (i) Unit I is negatively correlated with terrigenous end-members, which is due to its high organic matter content. (ii) Unit II can be separated into two parts, one positively correlated with Dim1 and, thus, to the detrital end-member, and one part that is characterized by a high Ca content. Values for the event layers identified as turbidites by Giguet-Covex et al. (2010) are almost exclusively positively correlated with the terrigenous end-member and especially with the upper part of this pole, while values obtained for the homogenite-type deposit are closer to the carbonate pole. From previous knowledge of sedimentary processes in Lake Bourget (Giguet-Covex et al., 2010; Arnaud et al., 2012; Jenny et al., 2013), and XRF and PCA results, we selected Ti as a proxy of detrital input from the river and Mn as a proxy of oxygenation of the water at the sediment interface. Indeed, when it is present at the base of an event layer and combined with a peak of a proxy of detrital input, a peak of Mn can be used as a proxy of oxygenation of the bottom water, and thus be used to detect and interpret flood layers.

4.4. Creation of interpreted flood event chronicle

The combination of Ti and Mn signals allowed to automatically provide a paleoflood record from the HSI event layer chronicle. Sixty-one layers present both Ti and Mn peaks and are identified as flood

events with a maximum thickness of 15.5 mm and a mean thickness of 5.6 mm. Twenty-one layers have only a peak of Mn, three layers only present a peak of Ti, and one layer does not present any peak of Ti and Mn. The homogenite-type deposit between 31.50 and 32.10 cm depth, linked to a seismic event that occurs close to the lake in 1822 AD (Chapron et al., 1999) is correctly discarded by the model (Fig. 3). Then, a flood chronicle was estimated with the 61 identified flood layers.

5. Discussion

5.1. Naked-eye versus HSI chronicles

Naked-eye observation could not be used to interpret the triggering mechanisms of event layers because different processes can lead to a turbiditic current into a lake. Then, from naked-eye observation, these deposits can only be considered as event layers interrupting continuous sedimentation. The HSI chronicle of event layers is compared to the naked-eye one to test the robustness of the developed methodology (Fig. 6A, B). The comparison is made on event frequency and cumulative thickness, both calculated as a sum of 10 cm. The HSI frequency is in great agreement with the naked-eye chronicle ($r = 0.86$ and $SE = 3.04$). The cumulative thickness derived from the SWIR camera is also very close to the one obtained from naked-eye observation ($r = 0.85$ and $SE = 1.94$). Thus, HSI differentiates event layers from continuous sedimentation. However, differences can be seen at the base and the top of the sediment section between the HSI and naked-eye chronicles. From 5.0 to 10.4 cm depth, the HSI chronicle presents a higher event frequency. This can be explained by the presence of varves (Fig. 4). Indeed, Unit I in Lake Bourget presents laminated sediment with a thin alternation of dark grey, light grey, and brown laminae that are hardly distinguishable visually. From 90 cm downwards, the HSI chronicle presents values of event frequency higher than expected compared to the naked-eye chronicle. This can be explained by the presence of an increasing number of very thin laminae that are non-distinguishable visually (< 1 mm). The higher number of thin layers detected by the HSI model (Fig. 4) explains higher values for the calculated cumulative thickness at the top and base of the core. Differences between HSI and naked-

eye frequencies are thus mainly linked to human identification bias and the intrinsic low resolution of naked-eye observation. However, if HSI identification presents some bias, the combination with XRF signals can correct this effect by discarding layers that do not present peaks of selected geochemical proxies. From HSI analysis, the detected layers can only be considered as event layers interrupting the continuous sedimentation, and the origin of those deposits cannot be discussed further as the geochemical properties used for their differentiation are not available from HSI data.

5.2. Automatic detection of flood layers

The (HSI+XRF) flood record is compared to the naked-eye one to test the robustness of the flood chronicle obtained (Figs. 6, 8). The frequency of this flood chronicle is highly comparable with the naked-eye chronicle, with r = 0.92 and SE = 1.27, as well as the cumulative thickness with r = 0.88 and SE = 1.61, respectively (Fig. 6). The (HSI+XRF) flood chronicle presents a better correlation with the naked-eye chronicle than the HSI chronicle alone. This can be explained by a potential over-detection of event layers by the HSI model that has been corrected by the addition of XRF signals. Indeed, a total of twenty-five deposits were discarded from the HSI model after incorporation of the XRF data interpretation. Compared to the HSI chronicle, the correlation between (HSI+XRF) and naked-eye frequencies is also higher at the top and the base of the core (Figs. 6, 8). Even if a higher number of floods are detected compare to the naked-eye chronicle, these events are confirmed by the XRF signals.

Twenty-one layers detected by the HSI model present a single Mn peak (Fig. 8), generally located at their base (Fig. 3). The homogenite-type deposit located between 31.50 and 32.10 cm depth and corresponding to the 1822 seismic event is one of them. A majority of these layers is probably linked to destabilization of slope sediments due to earthquake shaking or sediment overloading (Chapron et al., 1999). The slopes of Lake Bourget are enriched in authigenic carbonate and present a lower concentration in detrital elements (Arnaud et al., 2005). During sediment flows, water from shallower parts of the lake basin will be brought to the water-sediment interface where the

concentration in oxygen is lower and will then lead to precipitation of Fe and Mn oxy-hydroxides without increasing the input of detrital elements to the lake floor. Five of these layers are located in Unit I, corresponding to a varved organic gyttja linked to recent eutrophication of the lake. The presence of a Mn peak in these laminae can be the result of changes in the oxic/anoxic regime of the bottom water at the period of sediment deposition. All these statements confirm that the Mn signal alone cannot be used to distinguish the different triggering mechanisms of event layers in a lake presenting rapid changes in oxygenation state of bottom waters, by mixing processes, and it needs to be associated with a proxy of detrital or carbonate inputs. This also indicates that the combination of HSI model and XRF signals allows us to distinguish different triggering mechanisms for the detected event layers. Three event layers present a peak of Ti signal only (Fig. 8), which can be the result of the presence of a higher content of detrital elements without re-oxygenation of the deep water. This can be due to (i) a slide of previously deposited sediment from the delta, or (ii) a weak flood event, or more probably to (iii) a flood event occurring during the winter period, when water mixing in the lake occurs. At that period, underflows cannot cause re-oxygenation of deep water which explains the lack of a peak of Mn. However, these layers present a respective thickness of 1.7, 1.9 and 2.9 mm, and are distributed all along the sediment section (Fig. 8), then their removal from the chronicle will not have a significant impact. One other deposit does not present any peak of Mn or Ti and is located at 121 cm depth. This event layer is interpreted as an artifact linked to a change in sediment color and surface geometry at the end of the sediment section.

The quantile-quantile plots in Fig. 7 allow comparison of the event layer distributions identified by naked-eye logging with the (HSI+XRF) combination. The depth QQ-plot (Fig. **Error! Reference source not found.**7A), similar to the event frequency (Fig. 6), shows a good agreement between chronicles. The thickness QQ-plot (Fig. 7B) highlights differences with thicker deposits estimated by (HSI+XRF). This can be accounted for by (i) the curvature of the deposits and (ii) the eye resolution to see precisely the layer limits with colour variations, and this can also be seen with the millimeter steps of the naked eye chronicle.

Combining hyperspectral analysis and XRF data allows for a reliable semi-automatized flood chronicle (Fig. 8). This method can easily be used on other lake sediment sections to automatically detect flood layers as well as other types of event layers in a sediment sequence. The methodology could also be developed by combining other types of sensors, e.g. Visible and near-infrared, XRD, SEM, EDS. For an (HSI+XRF) combination, the only input parameters that will vary are the XRF signals chosen by the user for the interpretation of deposit triggers, requiring a comprehensive understanding of in-lake sedimentary processes. This method allows us to detect thinner deposits compare to a naked-eye observation, with 24 deposits thinner than 1 mm on a 121 cm-long sequence and a more robust thickness estimation (Fig. 8) used as flood intensity proxy in some lake systems. However, the trigger of these thin deposits cannot be characterized due to the XRF resolution of this study. This methodology presents a strong advantage in that it is fast and non-destructive. Its limitations may be the large amount (here 450 Mega octets for 1 meter of core analyzed) of data generated by hyperspectral analysis and by the requirements of a comprehensive understanding of the sedimentary processes in the studied lake. The over-detection of the event layers by the HSI can be corrected using XRF data. However, an interesting perspective for future work would be its development to automatically detect event layers related to other triggers (e.g., lake level fluctuations, snow avalanches, eruptions, sediment overloading on slopes or deltas, destabilization of slopes and deltas by seismic shaking) and their classification by types of trigger. We think that the proposed methodology is useful to more precisely documented sedimentary events and related natural hazards, but will also improve the workflow by reducing analysis time on long sediment sections, allowing the rapid study of a number of sequences.

6. Conclusions

This study presents the first semi-automatic method using multiproxy analyses to detect event layers in lake sediment in a fast and non-destructive way and allowing the direct interpretation of triggers of these deposits to create an event chronicle. One proximal sediment section of Lake Bourget was

described visually, analyzed with a SWIR hyperspectral camera and XRF core-scanner. A naked-eye chronicle was made to test the accuracy of the method. From HSI analysis, event layers that differ from continuous background sedimentation were detected and counted to build an event layer chronicle that is in good agreement with the naked-eye chronicle. From XRF analysis and previous knowledge, Ti and Mn signals were selected to disentangle flood layers from other event layers. Indeed, the Ti signal is directly linked to detrital inputs into the lake coming from the main tributaries, and Mn variations are linked to water-sediment interface oxygenation during a flood event. If the event layer detected by the HSI analysis presents a peak of Mn and Ti, then they were interpreted as flood-induced deposits and added to the flood chronicle. The accuracy of this flood chronicle was then tested by comparison with the naked-eye chronicle previously made on this sediment section. The very good agreement between these two chronicles allows validation of this new method that can be applied to other sediment sections to detect event layers and to produce interpreted chronicles, and more widely used for event layer identification in other lake systems.

Acknowledgments

Hyperspectral imaging was processed at the University of Normandie-Rouen and was funded by the Region Normandie, which supports the scientific consortium SCALE UMR CNRS 3730.

References

Arnaud, F., Revel, M., Chapron, E., Desmet, M., Tribovillard, N., 2005. 7200 years of Rhône river flooding activity in Lake Le Bourget, France: a high-resolution sediment record of NW Alps hydrology. The Holocene 15, 420–428.

Arnaud, F., Révillon, S., Debret, M., Revel, M., Chapron, E., Jacob, J., Giguet-Covex, C., Poulenard, J., Magny, M., 2012. Lake Bourget regional erosion patterns reconstruction reveals Holocene NW European Alps soil evolution and paleohydrology. Quat. Sci. Rev. 51, 81–92.

Barker, M., Rayens, W., 2003. Partial least squares for discrimination. J. Chemom. 17, 166–173.

Barnes, R.J., Dhanoa, M.S., Lister, S.J., 1989. Standard Normal Variate Transformation and De-Trending of Near-Infrared Diffuse Reflectance Spectra. Appl. Spectrosc. 43, 772–777.

Blöschl, G., Hall, J., Viglione, A., Perdigão, R.A., Parajka, J., Merz, B., Lun, D., Arheimer, B., Aronica, G.T., Bilibashi, A., 2019. Changing climate both increases and decreases European river floods. Nature 573, 108–111.

Butz, C., Grosjean, M., Fischer, D., Wunderle, S., Tylmann, W., Rein, B., 2015. Hyperspectral imaging spectroscopy: a promising method for the biogeochemical analysis of lake sediments. J. Appl. Remote Sens. 9, 096031.

Butz, C., Grosjean, M., Goslar, T., Tylmann, W., 2017. Hyperspectral imaging of sedimentary bacterial pigments: a 1700-year history of meromixis from varved Lake Jaczno, northeast Poland. J. Paleolimnol. 58, 57–72.

Chapron, E., Arnaud, F., Noël, H., Revel, M., Desmet, M., Perdereau, L., 2005. Rhone River flood deposits in Lake Le Bourget: a proxy for Holocene environmental changes in the NW Alps, France. Boreas 34, 404–416.

Chapron, E., Beck, C., Pourchet, M., Deconinck, J.-F., 1999. 1822 earthquake-triggered homogenite in Lake Le Bourget (NW Alps). Terra Nova 11, 86–92.

Chapron, E., Desmet, M., De Putter, T., Loutre, M.F., Beck, C., Deconinck, J.-F., 2002. Climatic variability in the northwestern Alps, France, as evidenced by 600 years of terrigenous sedimentation in Lake Le Bourget. The Holocene, The Holocene 12, 177–185.

Corella, J.P., Benito, G., Wilhelm, B., Montoya, E., Rull, V., Vegas-Vilarrúbia, T., Valero-Garcés, B.L., 2019. A millennium-long perspective of flood-related seasonal sediment yield in Mediterranean watersheds. Glob. Planet. Change 177, 127–140.

Davies, S.J., Lamb, H.F., Roberts, S.J., 2015. Micro-XRF core scanning in palaeolimnology: recent developments. In: (Eds) Micro-XRF Studies of Sediment Cores. Springer, pp. 189–226.

Davison, W., 1993. Iron and manganese in lakes. Earth-Sci. Rev. 34, 119–163.

Debret, M., Chapron, E., Desmet, M., Rolland-Revel, M., Magand, O., Trentesaux, A., Bout-Roumazeille, V., Nomade, J., Arnaud, F., 2010. North western Alps Holocene paleohydrology recorded by flooding activity in Lake Le Bourget, France. Quat. Sci. Rev. 29, 2185–2200.

Elbaz-Poulichet, F., Sabatier, P., Dezileau, L., Freydier, R., 2014. Sedimentary record of V, U, Mo and Mn in the Pierre-Blanche lagoon (Southern France)–Evidence for a major anoxia event during the Roman period. The Holocene 24, 1384–1392.

Evin, G., Wilhelm, B., Jenny, J.-P., 2019. Flood hazard assessment of the Rhône River revisited with reconstructed discharges from lake sediments. Glob. Planet. Change 172, 114–123.

Giguet-Covex, C., Arnaud, F., Enters, D., Poulenard, J., Millet, L., Francus, P., David, F., Rey, P.-J., Wilhelm, B., Delannoy, J.-J., 2012. Frequency and intensity of high-altitude floods over the last 3.5 ka in northwestern French Alps (Lake Anterne). Quat. Res. 77, 12–22.

Giguet-Covex, C., Arnaud, F., Poulenard, J., Enters, D., Reyss, J.-L., Millet, L., Lazzaroto, J., Vidal, O., 2010. Sedimentological and geochemical records of past trophic state and hypolimnetic anoxia in large, hard-water Lake Bourget, French Alps. J. Paleolimnol. 43, 171–190.

Gilli, A., Anselmetti, F.S., Glur, L., Wirth, S.B., 2013. Lake sediments as archives of recurrence rates and intensities of past flood events. In: (Eds) Dating Torrential Processes on Fans and Cones. Springer, pp. 225–242.

Glur, L., Wirth, S.B., Büntgen, U., Gilli, A., Haug, G.H., Schär, C., Beer, J., Anselmetti, F.S., 2013. Frequent floods in the European Alps coincide with cooler periods of the past 2500 years. Sci. Rep. 3, 2770. https://doi.org/10.1038/srep02770

Hirabayashi, Y., Mahendran, R., Koirala, S., Konoshima, L., Yamazaki, D., Watanabe, S., Kim, H., Kanae, S., 2013. Global flood risk under climate change. Nat. Clim. Change 3, 816.

Jacq, K., Giguet-Covex, C., Sabatier, P., Perrette, Y., Fanget, B., Coquin, D., Debret, M., Arnaud, F., 2019a. High-resolution grain size distribution of sediment core with hyperspectral imaging. Sediment. Geol. 393–394, 105536.

Jacq, Kevin, Martinez-Lamas, R., Van Exem, A., Debret, M., 2020. Hyperspectral core-logger image acquisition. https://www.protocols.io/view/hyperspectral-core-logger-image-acquisition-bikckcswJacq, K., Perrette, Y., Fanget, B., Sabatier, P., Coquin, D., Martinez-Lamas, R., Debret, M., Arnaud, F., 2019b. High-resolution prediction of organic matter concentration with hyperspectral imaging on a sediment core. Sci. Total Environ. 663, 236–244.

Jacq, Kévin, William, R., Alexandre, B., Didier, C., Bernard, F., Perrette, Y., Sabatier, P., Bruno, W., Maxime, D., Arnaud, F., 2020. Sedimentary structures discriminations with hyperspectral imaging on sediment cores (preprint). EarthArXiv.

Jenny, J.-P., Arnaud, F., Dorioz, J.-M., Covex, C.G., Frossard, V., Sabatier, P., Millet, L., Reyss, J.-L., Tachikawa, K., Bard, E., 2013. A spatiotemporal investigation of varved sediments highlights the dynamics of hypolimnetic hypoxia in a large hard-water lake over the last 150 years. Limnol. Oceanogr. 58, 1395–1408.

Jenny, J.-P., Wilhelm, B., Arnaud, F., Sabatier, P., Covex, C.G., Melo, A., Fanget, B., Malet, E., Ployon, E., Perga, M.E., 2014. A 4D sedimentological approach to reconstructing the flood frequency and intensity of the Rhône River (Lake Bourget, NW European Alps). J. Paleolimnol. 51, 469–483.

Lampinen, H.M., Laukamp, C., Occhipinti, S.A., Hardy, L., 2019. Mineral footprints of the Paleoproterozoic sediment-hosted Abra Pb-Zn-Cu-Au deposit Capricorn Orogen, Western Australia. Ore Geol. Rev. 104, 436–461.

Merz, B., Aerts, J., Arnbjerg-Nielsen, K., Baldi, M., Becker, A., Bichet, A., Blöschl, G., Bouwer, L.M., Brauer, A., Cioffi, F., 2014. Floods and climate: emerging perspectives for flood risk assessment and management. Nat. Hazards Earth Syst. Sci. 14, 1921–1942.

Millet, L., Giguet-Covex, C., Verneaux, V., Druart, J.-C., Adatte, T., Arnaud, F., 2010. Reconstruction of the recent history of a large deep prealpine lake (Lake Bourget, France) using subfossil chironomids, diatoms, and organic matter analysis: towards the definition of a lake-specific reference state. J. Paleolimnol. 44, 963–978.

Moreno, A., Valero-Garcés, B.L., González-Sampériz, P., Rico, M., 2008. Flood response to rainfall variability during the last 2000 years inferred from the Taravilla Lake record (Central Iberian Range, Spain). J. Paleolimnol. 40, 943–961.

Nicoud, G., Monjuvent, G., Maillet-Guy, G., 1987. Contrôle du comblement quaternaire des vallées alpines du nord par la dynamique lacustre. Géologie Alpine, Mém. h.s. n°13. pp. 457–468. insu-00512339

Noren, A.J., Bierman, P.R., Steig, E.J., Lini, A., Southon, J., 2002. Millennial-scale storminess variability in the northeastern United States during the Holocene epoch. Nature 419, 821–824.

Rapuc, W., Sabatier, P., Andrič, M., Crouzet, C., Arnaud, F., Chapron, E., Šmuc, A., Develle, A.-L., Wilhelm, B., Demory, F., 2018. 6600 years of earthquake record in the Julian Alps (Lake Bohinj, Slovenia). Sedimentology 65, 1777–1799.

Rapuc, W., Sabatier, P., Arnaud, F., Palumbo, A., Develle, A.-L., Reyss, J.-L., Augustin, L., Régnier, E., Piccin, A., Chapron, E., Dumoulin, J.-P., von Grafenstein, U., 2019. Holocene-long record of flood frequency in the Southern Alps (Lake Iseo, Italy) under human and climate forcing. Glob. Planet. Change 175, 160–172.

Revel-Rolland, M., Arnaud, F., Chapron, E., Desmet, M., Givelet, N., Alibert, C., McCulloch, M., 2005. Sr and Nd isotopes as tracers of clastic sources in Lake Le Bourget sediment (NW Alps, France) during the Little Ice Age: Palaeohydrology implications. Chem. Geol. 224, 183–200.

Sabatier, P., Dezileau, L., Briqueu, L., Colin, C., Siani, G., 2010. Clay minerals and geochemistry record from northwest Mediterranean coastal lagoon sequence: Implications for paleostorm reconstruction. Sediment. Geol. 228, 205–217.

Sabatier, P., Wilhelm, B., Ficetola, G.F., Moiroux, F., Poulenard, J., Develle, A.-L., Bichet, A., Chen, W., Pignol, C., Reyss, J.-L., Gielly, L., Bajard, M., Perrette, Y., Malet, E., Taberlet, P., Arnaud, F., 2017. 6-kyr record of flood frequency and intensity in the western Mediterranean Alps – Interplay of solar and temperature forcing. Quat. Sci. Rev. 170, 121–135.

Sauerbrey, M.A., Juschus, O., Gebhardt, A.C., Wennrich, V., Nowaczyk, N.R., Melles, M., 2013. Mass movement deposits in the 3.6 Ma sediment record of Lake El'gygytgyn, Far East Russian Arctic. Clim. Past 9, 1949–1967.

Savitzky, Abraham., Golay, M.J.E., 1964. Smoothing and Differentiation of Data by Simplified Least Squares Procedures. Anal. Chem. 36, 1627–1639.

Schneider, T., Rimer, D., Butz, C., Grosjean, M., 2018. A high-resolution pigment and productivity record from the varved Ponte Tresa basin (Lake Lugano, Switzerland) since 1919: insight from an approach that combines hyperspectral imaging and high-performance liquid chromatography. J. Paleolimnol. 60, 381–398.

Speta, M., Rivard, B., Feng, J., 2018. Shortwave infrared (1.0–2.5 µm) hyperspectral imaging of the Athabasca West Grand Rapids Formation oil sands. AAPG Bull. 102, 1671–1683.

Sturm, M., Matter, A., 1978. Turbidites and varves in Lake Brienz (Switzerland): deposition of clastic detritus by density currents. Mod. Anc. Lake Sediments 147–168.

Tusa, L., Andreani, L., Khodadadzadeh, M., Contreras, C., Ivascanu, P., Gloaguen, R., Gutzmer, J., 2019. Mineral Mapping and Vein Detection in Hyperspectral Drill-Core Scans: Application to Porphyry-Type Mineralization. Minerals 9, 122.

Van Exem, A., Debret, M., Coparo, Y., Vannière, B., Sabatier, P., Marcotte, S., Laignel, B., Reyss, J.-L., Desmet, M., 2018. Hyperspectral core logging for fire reconstruction studies. J. Paleolimnol. 59, 297–308.

Vannière, B., Magny, M., Joannin, S., Simonneau, A., Wirth, S.B., Hamann, Y., Chapron, E., Gilli, A., Desmet, M., Anselmetti, F.S., 2013. Orbital changes, variation in solar activity and increased anthropogenic activities: controls on the Holocene flood frequency in the Lake Ledro area, Northern Italy. Clim. Past 9, 1193–1209.

Wilhelm, B., Arnaud, F., Sabatier, P., Crouzet, C., Brisset, E., Chaumillon, E., Disnar, J.-R., Guiter, F., Malet, E., Reyss, J.-L., Tachikawa, K., Bard, E., Delannoy, J.-J., 2012. 1400 years of extreme

precipitation patterns over the Mediterranean French Alps and possible forcing mechanisms. Quat. Res. 78, 1–12.

Wilhelm, B., Arnaud, F., Sabatier, P., Magand, O., Chapron, E., Courp, T., Tachikawa, K., Fanget, B., Malet, E., Pignol, C., Bard, E., Delannoy, J.J., 2013. Palaeoflood activity and climate change over the last 1400 years recorded by lake sediments in the north-west European Alps. J. Quat. Sci. 28, 189–199.

Wilhelm, B., Cánovas, J.A.B., Macdonald, N., Toonen, W.H.J., Baker, V., Barriendos, M., Benito, G., Brauer, A., Corella, J.P., Denniston, R., Glaser, R., Ionita, M., Kahle, M., Liu, T., Luetscher, M., Macklin, M., Mudelsee, M., Munoz, S., Schulte, L., George, S.S., Stoffel, M., Wetter, O., 2019. Interpreting historical, botanical, and geological evidence to aid preparations for future floods. WIREs Water 6, e1318. https://doi.org/10.1002/wat2.1318

Wilhelm, B., Vogel, H., Anselmetti, F.S., 2017. A multi-centennial record of past floods and earthquakes in Valle d'Aosta, Mediterranean Italian Alps. Nat. Hazards Earth Syst. Sci. 17, 613.

Wilhelm, B., Vogel, H., Crouzet, C., Etienne, D., Anselmetti, F.S., 2016. Frequency and intensity of palaeofloods at the interface of Atlantic and Mediterranean climate domains. Clim. Past 12, 299–316.

Wirth, S.B., Glur, L., Gilli, A., Anselmetti, F.S., 2013. Holocene flood frequency across the Central Alps–solar forcing and evidence for variations in North Atlantic atmospheric circulation. Quat. Sci. Rev. 80, 112–128.

Wold, S., Ruhe, A., Wold, H., Dunn III, W.J., 1984. The Collinearity Problem in Linear Regression. The Partial Least Squares (PLS) Approach to Generalized Inverses. SIAM J. Sci. Stat. Comput. 5, 735–743.

Figure 1. Location of Lake Bourget in the European Alps, its bathymetry, and location of the coring site (LDB17-P11).

Figure 2. Summary of the methodology developed for the semi-automatic detection and interpretation of flood event layers in lake sediments based on the combination of hyperspectral and XRF data and the comparison with a naked eye study.

Figure 3. Details of RGB images and SWIR classification map, associated with summed profile derived from hyperspectral imaging model. The orange line shows the detected event layers from HSI model. In the Lake Bourget example, Mn and Ti signals were chosen to interpret flood layers. Location and thickness of flood layers detected by the combination of HSI and XRF data are represented by purple rectangles.

Figure 4. Main results obtained on LDB17-P11A sediment section : the picture of the core, the stratigraphic log with the turbidite-type deposits identified by a visual description of the core represented in grey and the homogenite-type deposit in white, the main XRF data used hereafter (Ti, Fe, Mn, K, Ca and Zr/K ratio), the picture of the core in RGB colors, the discrimination model showing event layers identified using hyperspectral camera SWIR.

Figure 5. Variable and individual factor maps from the PCA. (A) Variable factor map with three end-members (terrigenous, organic matter, and carbonates). (B) Individual factor map with sedimentological units added as an illustrative variable.

Figure 6. Comparison between the different models of the event layers and flood chronicles obtained, the naked-eye models are represented in blue, the HSI chronicle in red and the combination HSI+XRF in green. (A) Frequency of events calculated as the sum of events layers per 10 cm. (B) Cumulative thickness derived from the above chronicles. N = number of event layers detected, r = correlation coefficient, SE = standard error.

Figure 7. Quantile-Quantile plot to compare the naked-eye and the HSI-XRF distributions of the (A) depth and the (B) thickness.

Figure 8. Synthesis of data used to produce the flood chronicle (naked-eye description, the event layers identified using hyperspectral camera SWIR and XRF data) and the main results obtained from the combination of XRF and HSI data (thickness of the event layers deposits, flood layers chronicle). Grey and blue shadings correspond to event layers identified visually.

Declaration of competing interest

The authors declare that they have no known competing financial interests or personal relationships that could have appeared to influence the work reported in this paper.

Highlights

- Common methods of flood detection in lake sediments present bias
- Hyperspectral and geochemical analyses allow automatic detection of flood layers
- Flood occurrence and thickness are in good agreement with previous chronicles
- This new method increases efficiency and robustness of paleoflood reconstructions
- It can be applied to identify any specific layers in lake sediments

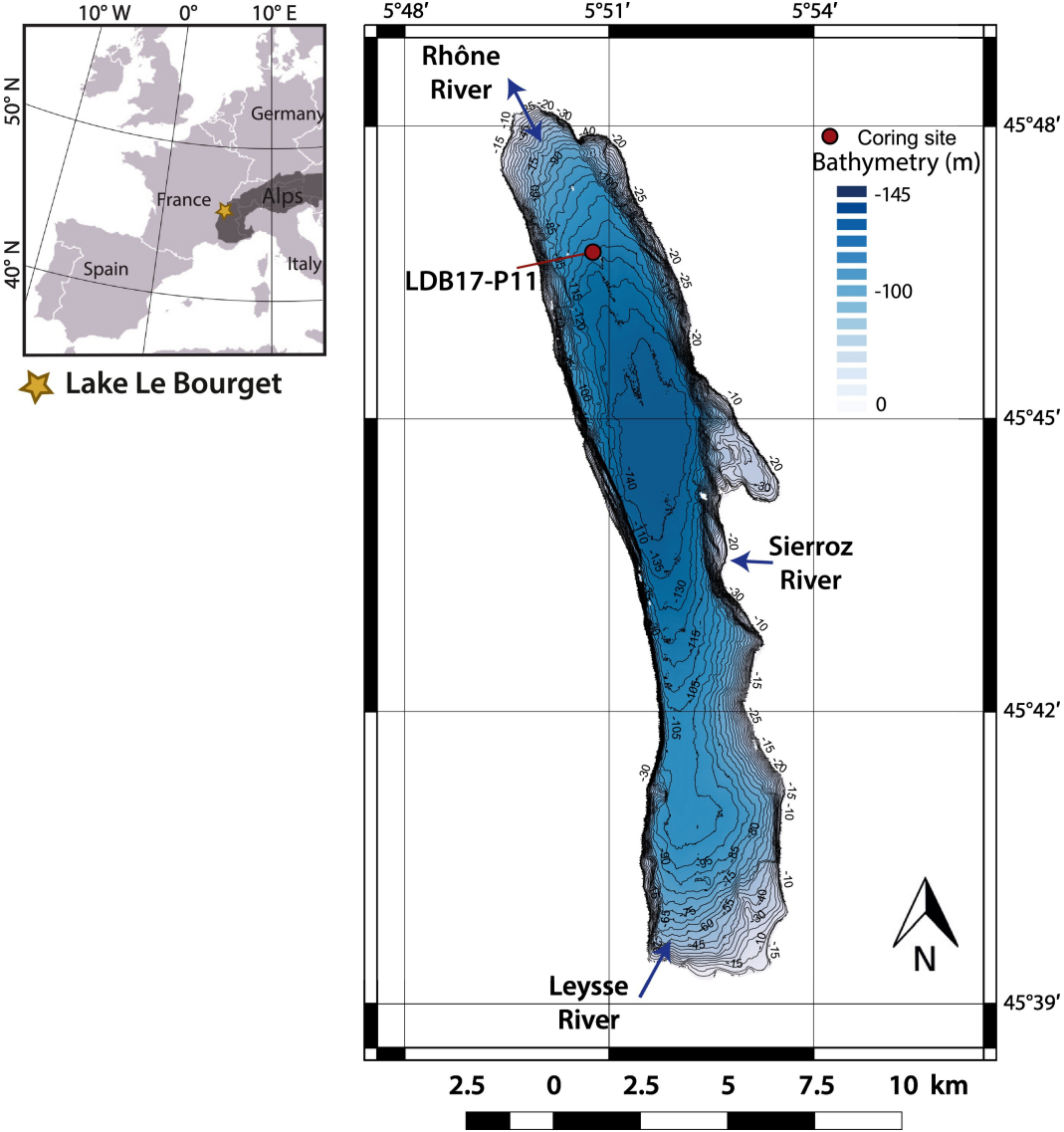
10° W
0°
10° E
50° N
40° N
Germany
France
Alps
Spain
Italy
Lake Le Bourget
5°48′
5°51′
5°54′
45°48′
45°45′
45°42′
45°39′
Rhône River
Coring site
Bathymetry (m)
-145
-100
0
LDB17-P11
Sierroz River
Leysse River
N
2.5
0
2.5
5
7.5
10 km

Figure 1

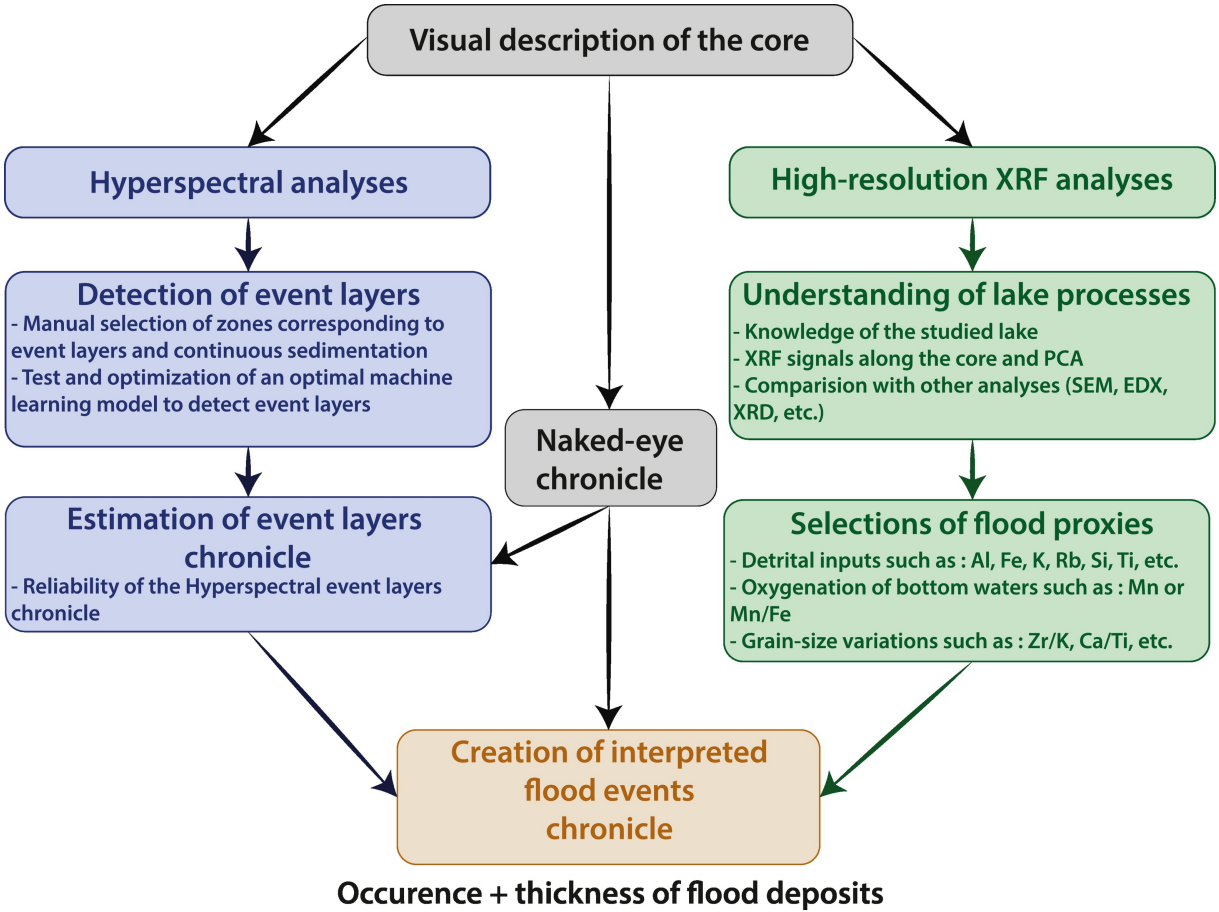
Visual description of the core
Hyperspectral analyses
Detection of event layers
- Manual selection of zones corresponding to event layers and continuous sedimentation
- Test and optimization of an optimal machine learning model to detect event layers
Estimation of event layers chronicle
- Reliability of the Hyperspectral event layers chronicle
Naked-eye chronicle
High-resolution XRF analyses
Understanding of lake processes
- Knowledge of the studied lake
- XRF signals along the core and PCA
- Comparision with other analyses (SEM, EDX, XRD, etc.)
Selections of flood proxies
- Detrital inputs such as : Al, Fe, K, Rb, Si, Ti, etc.
- Oxygenation of bottom waters such as : Mn or Mn/Fe
- Grain-size variations such as : Zr/K, Ca/Ti, etc.
Creation of interpreted flood events chronicle
Occurence + thickness of flood deposits

Figure 2

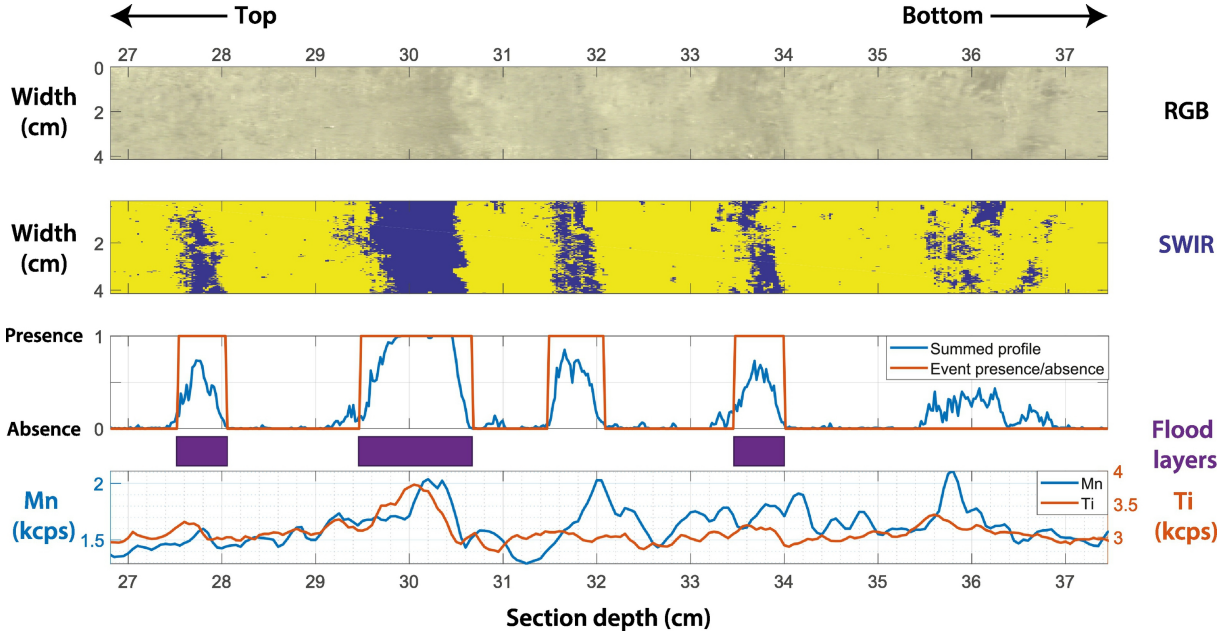
Top
Bottom
27
28
29
30
31
32
33
34
35
36
37
Width (cm)
0
2
4
RGB
Width (cm)
2
4
SWIR
Presence
Absence
1
0
Summed profile
Event presence/absence
Flood layers
Mn (kcps)
2
1.5
Mn
Ti
4
3.5
3
Ti (kcps)
Section depth (cm)

Figure 3

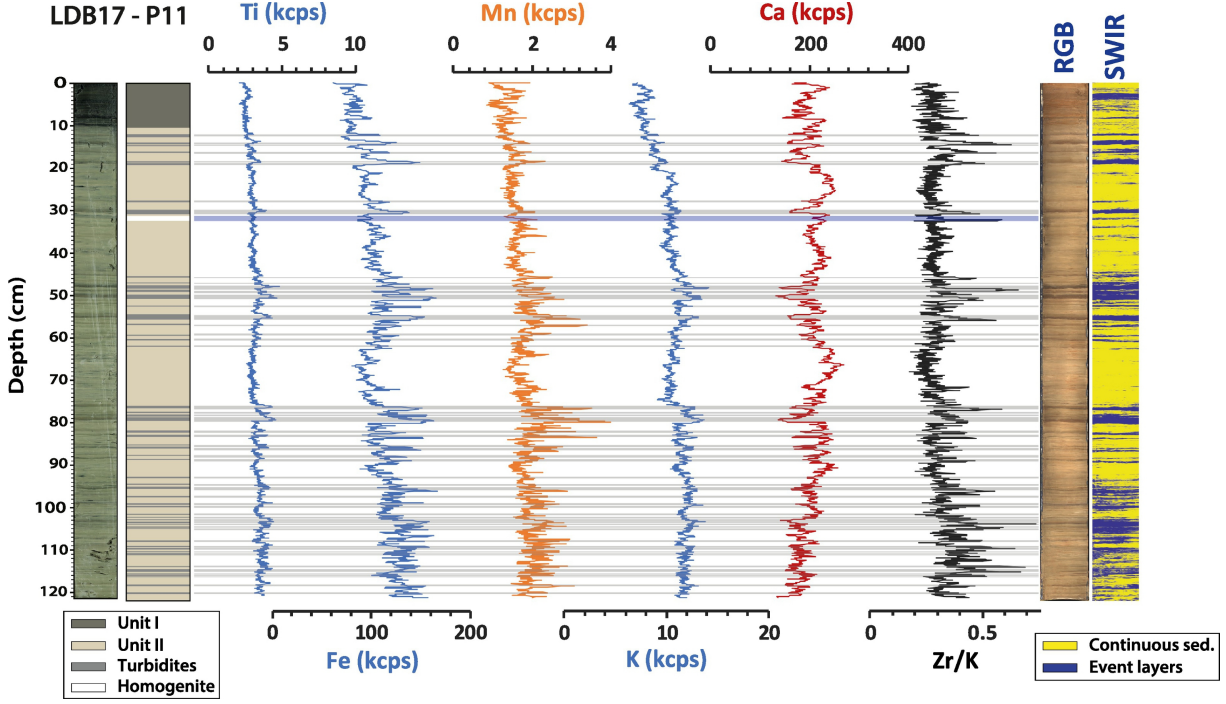
LDB17 - P11
Ti (kcps)
Mn (kcps)
Ca (kcps)
RGB
SWIR
Depth (cm)
Unit I
Unit II
Turbidites
Homogenite
Fe (kcps)
K (kcps)
Zr/K
Continuous sed.
Event layers

Figure 4

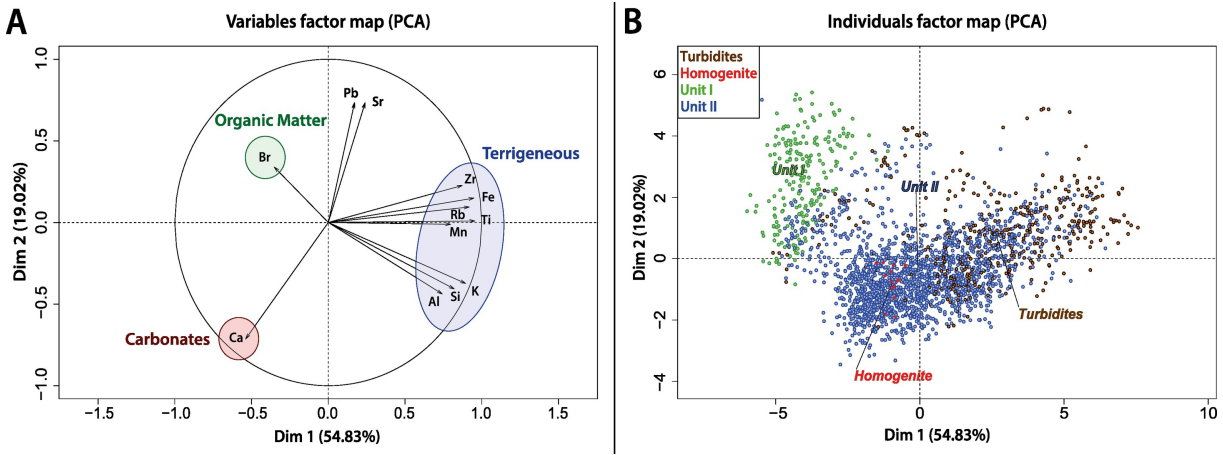
A
Variables factor map (PCA)
Organic Matter
Terrigeneous
Carbonates
Pb
Sr
Br
Zr
Fe
Rb
Ti
Mn
Al
Si
K
Ca
Dim 2 (19.02%)
Dim 1 (54.83%)
B
Individuals factor map (PCA)
Turbidites
Homogenite
Unit I
Unit II
Dim 2 (19.02%)
Dim 1 (54.83%)

Figure 5

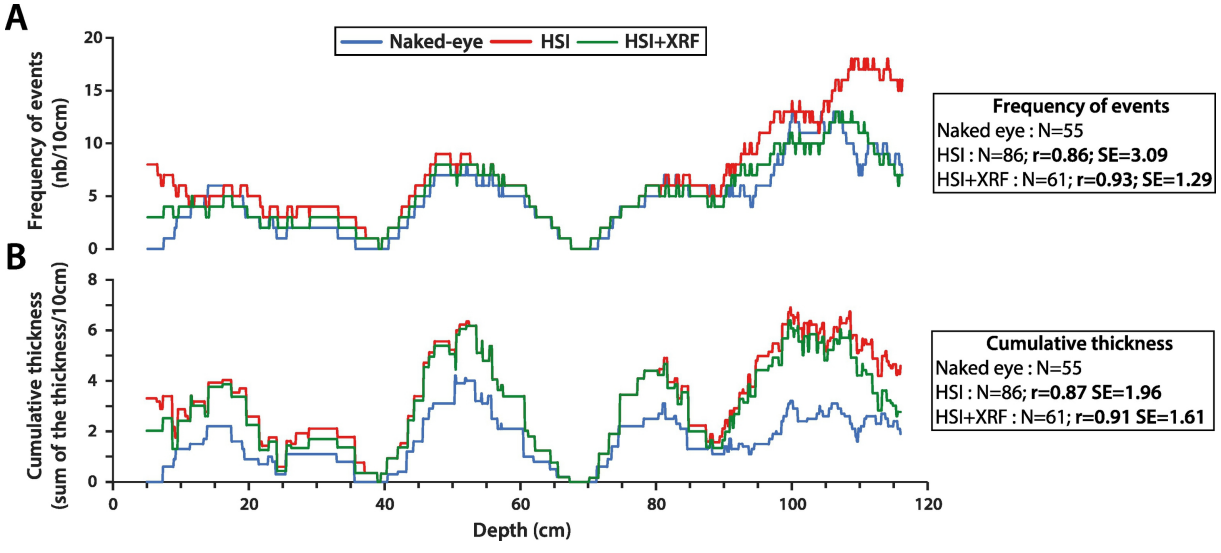
A
Naked-eye
HSI
HSI+XRF
Frequency of events (nb/10cm)
0
5
10
15
20
Frequency of events
Naked eye : N=55
HSI : N=86; r=0.86; SE=3.09
HSI+XRF : N=61; r=0.93; SE=1.29
B
Cumulative thickness (sum of the thickness/10cm)
0
2
4
6
8
Cumulative thickness
Naked eye : N=55
HSI : N=86; r=0.87 SE=1.96
HSI+XRF : N=61; r=0.91 SE=1.61
0
20
40
60
80
100
120
Depth (cm)

Figure 6

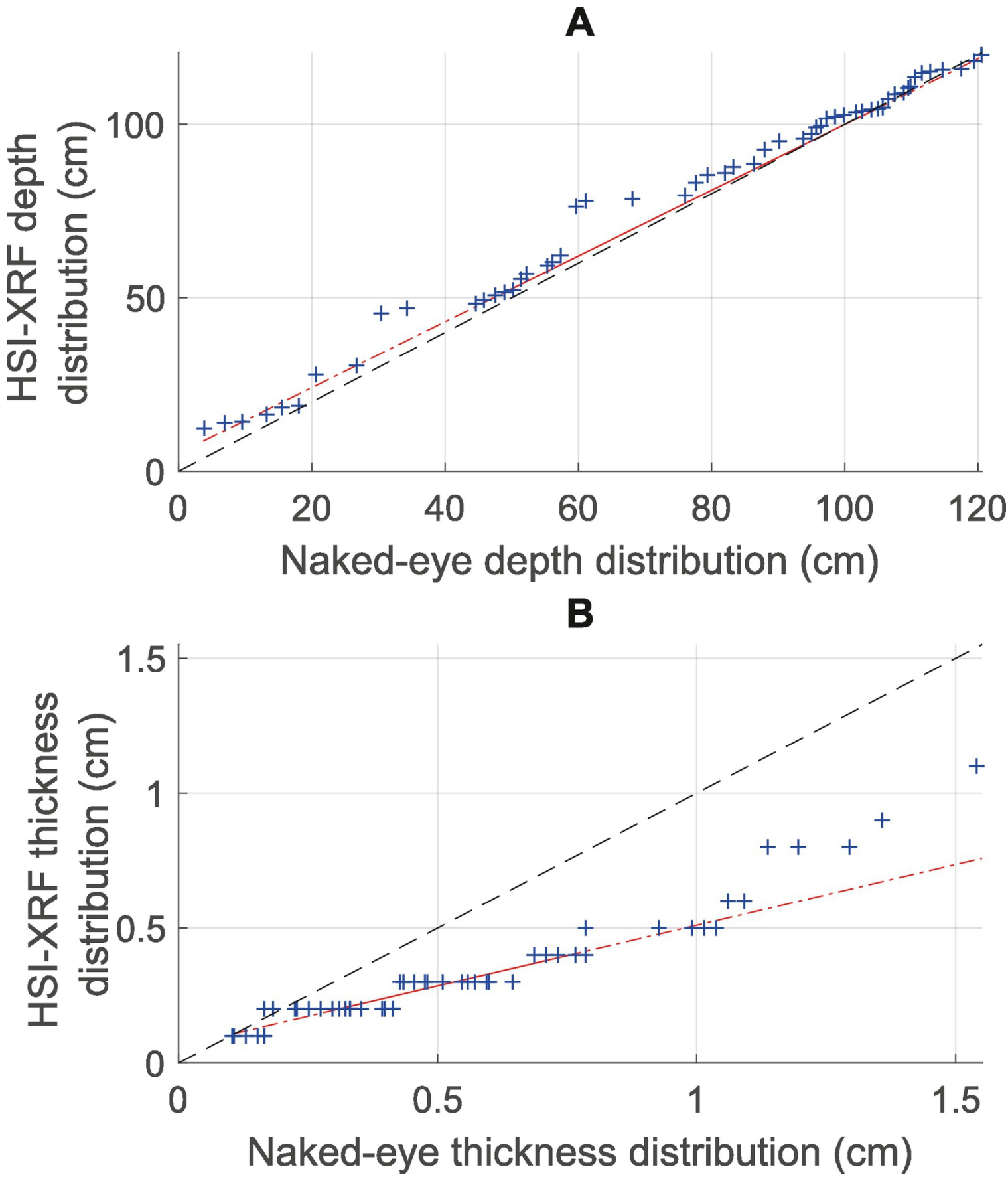
A
HSI-XRF depth distribution (cm)
0
50
100
0
20
40
60
80
100
120
Naked-eye depth distribution (cm)
B
HSI-XRF thickness distribution (cm)
0
0.5
1
1.5
0
0.5
1
1.5
Naked-eye thickness distribution (cm)

Figure 7

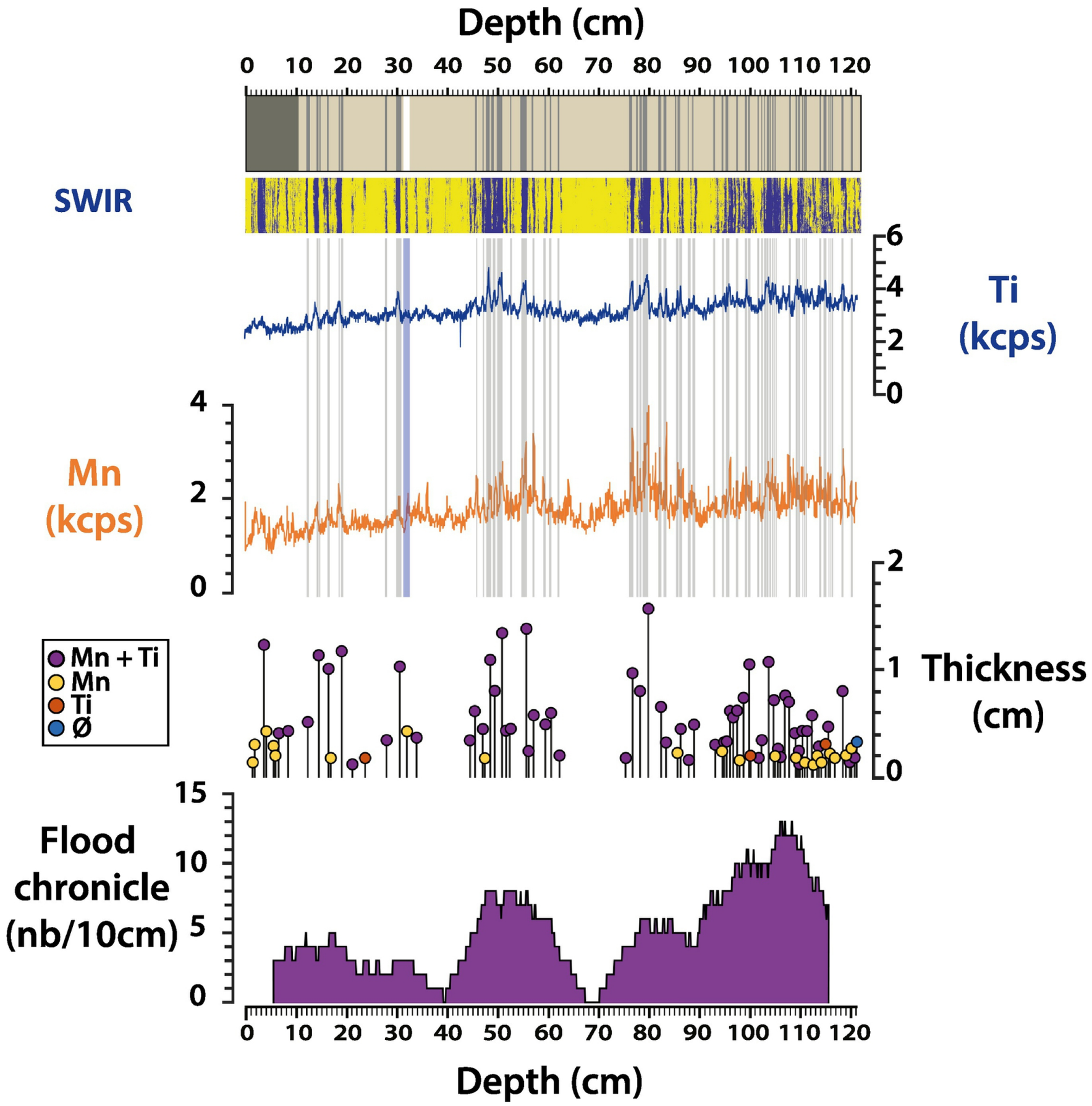
Depth (cm)
0 10 20 30 40 50 60 70 80 90 100 110 120
SWIR
Ti (kcps)
6
4
2
0
Mn (kcps)
4
2
0
Mn + Ti
Mn
Ti
Ø
2
1
0
Thickness (cm)
Flood chronicle (nb/10cm)
15
10
5
0
0 10 20 30 40 50 60 70 80 90 100 110 120
Depth (cm)

Figure 8